In: Brain Research Journal 2007, Volume 1, Issue 4 ISSN 1935-2875
Editor:Frank Columbus, pp.

SEGMENTATION PROPAGATION FROM DEFORMABLE ATLASES FOR BRAIN MAPPING AND ANALYSIS

Marius George Linguraru*[1], Tom Vercauteren[2,3], Mauricio Reyes-Aguirre[4], Miguel Ángel González Ballester[4] and Nicholas Ayache[2]

[1]Diagnostic Radiology Department, Clinical Center, National Institutes of Health, Bethesda MD, USA
[2]Epidaure/Asclepios Research Group, INRIA, Sophia Antipolis, France
[3]Mauna Kea Technologies, Paris, France
[4]MEM Research Center, Institute for Surgical Technology and Biomechanics, University of Bern, Switzerland

ABSTRACT

Magnetic resonance imaging (MRI) is commonly employed for the depiction of soft tissues, most notably the human brain. Computer-aided image analysis techniques lead to image enhancement and automatic detection of anatomical structures. However, the intensity information contained in images does not often offer enough contrast to robustly obtain a good detection of all internal brain structures, not least the deep gray matter nuclei. We propose digital atlases that deform to fit the image data to be analyzed. In this application, deformable atlases are employed for the detection and segmentation of brain nuclei, to allow analysis of brain structures. Our fully automatic technique is based on a combination of rigid, affine and non-linear registration, a priori information on key anatomical landmarks and propagation of the information of the atlas. The Internet Brain Segmentation Repository (IBSR) data provide manually segmented brain data. Using prior anatomical knowledge in local brain areas from a randomly chosen brain scan (atlas), a first estimation of the deformation fields is calculated by affine registration. The image alignment is refined through a non-linear transformation to correct the segmentation of nuclei. The local segmentation results are greatly improved. They are robust over the patient data and in accordance with the clinical ground truth. Validation of results is assessed by comparing the automatic segmentation of deep gray nuclei by the proposed method with manual segmentation. The technique offers the accurate segmentation of difficultly identifiable brain structures in conjuncture with deformable atlases. Such automated processes allow the study of large image databases and provide consistent measurements over the data. The method has a wide range of clinical

* E-mail: lingurarum@mail.nih.gov

applications of high impact that span from size and intensity quantification to comprehensive (anatomical, functional, dynamic) analysis of internal brain structures.

Keywords: MRI, brain, gray matter nuclei, atlas, registration, deformation, segmentation.

1. INTRODUCTION

The advent of medical imaging modalities such as X-ray, ultrasound, computed tomography (CT) and magnetic resonance imaging (MRI) has greatly improved the diagnosis of human diseases. Until recently, the most common procedure to analyze imaging data was visual inspection on printed support. In the last decade, computer-aided medical image analysis techniques have been employed to provide a better insight into the acquired image data [Duncan and Ayache 2000]. Such techniques allow for quantitative, reproducible observation of the patient condition. Furthermore, the computing power of modern machines can be used to combine information from several images of the same patient (i.e. image fusion) or add prior information from a database of images.

In this chapter, we present a fully automated medical image analysis technique aimed at the detection of internal brain structures from MRI data. Such automated processes allow the study of large image databases and provide consistent measurements over the data. In our case, we employ a priori anatomical knowledge in the form of digital brain atlases.

Relevant background information about MRI and brain anatomy is provided next. In Methods we describe the different components of our image processing framework, which segments and quantifies internal brain structures by propagating deformable models of internal nuclei. Finally, results are presented and the algorithm is assessed.

1.1. Magnetic Resonance Imaging

MRI has become a leading technique widely used for imaging soft human tissue. Its applications are extended over all parts of the human body and it represents the most common visualization method of human brain. Images are generated by measuring the behavior of soft tissue under a magnetic field. Under such conditions, water protons enter a higher energy state when a radio-frequency pulse is applied and this energy is re-emitted when the pulse stops (a property known as resonance) [Hornak]. A coil is used to measure this energy, which is proportional to the quantity of water protons and local biochemical conditions. Thus, different tissues give different intensities in the final MR image. From the brain MRI perspective, this quality makes possible the segmentation of the three main tissue classes within the human skull: gray matter (GM), white matter (WM) and cerebrospinal fluid (CSF). Their accurate segmentation and sub-classification remains a challenging task in the clinical environment.

The relative contrast between brain tissues is not a constant in MR imaging. In most medical imaging applications, little can be done about the appearance of anatomically distinct areas relative to their surroundings. In MRI, the choice of the strength and timing of the radio-frequency pulses, known as the MRI sequence [Stark et al.1999], can be employed to

highlight some type of tissue or image out another, according to the clinical application. However, the presence of artifacts due to magnetic field inhomogeneity (bias fields) and movement artifacts may hamper the delineation of GM versus WM and CSF and make their depiction difficult [Fennema-Notestine et al. 2006; Guillemaud et al.1997; Han et al. 2006; Sled et al.1998; Van Leemput et al. 1999].

Several MRI sequences are used in common clinical practice. T1-weighted MRI offers the highest contrast between the brain soft tissues and is arguably the most popular MR acquisition technique used for brain diagnosis. On the contrary, T2-weighted and Proton Density (PD) images exhibit very low contrast between GM and WM, but high contrast between CSF and brain parenchyma. In other MRI sequences, like the Fluid Attenuated Inversion Recovery (FLAIR) sequence, the CSF is eliminated from the image in an adapted T1 or T2 sequence. More about these specific MRI sequences and their variations can be found in [Brown and Semelka 1999].

MR images depict a 3D volume where the organ or part of the body of interest is embedded. This information can be used to build a 3D representation of the structure of interest. This applies both to 2D sequences, where images are acquired in slices, and to the recently developed 3D sequences, where the data are captured in the 3D Fourier space, rather than each slice being captured separately in the 2D Fourier space [Brown and Semelka 1999; Stark et al. 1999].

1.2. Deep Gray Matter Nuclei

The neurons that build up the human brain are composed of a cellular body and an axon. The latter projects its dendritic connections to other neurons in remote cerebral regions. In essence, gray matter corresponds to the cellular bodies, whereas the axons constitute the white matter. Cerebral gray matter is mainly concentrated in the outer surface of the brain (cortex), but several internal GM structures exist, as seen in Figure 1. These are known as deep gray matter nuclei and they play a central role in the intellectual capabilities of the human brain. Additionally, deep brain gray matter nuclei are relevant to a set of clinical conditions, such as Parkinson's and Creutzfeldt-Jakob diseases [Summerfield et al. 2005; Linguraru et al. 2006]. The size and appearance of gray nuclei can be indicators of abnormality. However, their detection in MRI data sets remains a challenging task, due to their small size, partial volume effects [González Ballester et al.2002], anatomical variability, lack of white matter-gray matter contrast in some sequences and movement artifacts. A methodology for the robust detection of deep brain gray matter nuclei in multi-sequence MRI is presented in this chapter.

1.3. Segmentation Based on Deformable Atlases

Brain atlases are images that have been segmented and thus contain information about the position and shape of each structure. Such atlases can be binary (1 for the location of a structure and 0 for "outside") or probabilistic, in which case the values correspond to the probability of a voxel containing the structure of interest. In order to locate such structures in a given patient image, the atlas image is deformed to match the shape of the patient brain

through registration. Depending on the number of degrees of freedom and the type of geometric deformation allowed, registration can be rigid, affine, or non-linear (a deformation field specifying the displacement applied to each point).

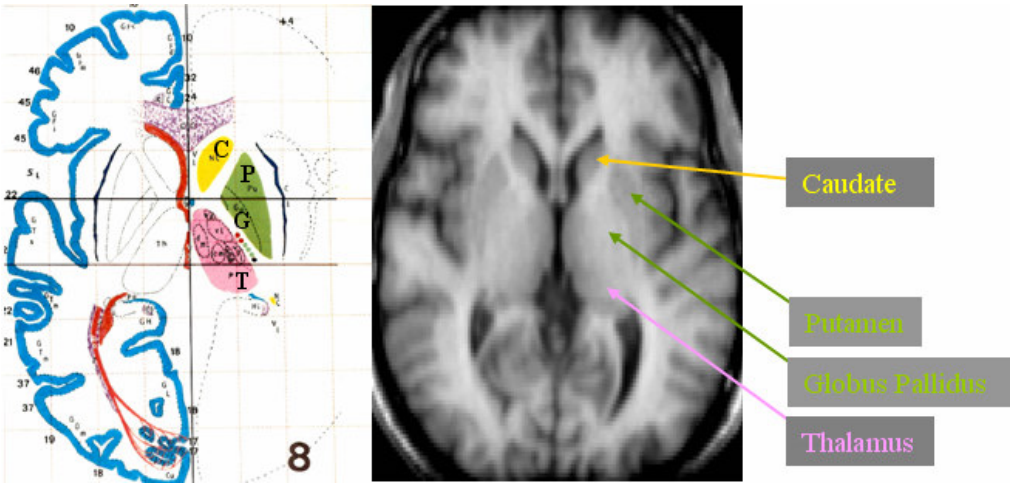

Figure 1. The map of gray matter nuclei in axial view. To the left, an annotated map of deep gray matter internal nuclei reproduced from the Talairach and Tournoux atlas [Talairach and Tournoux 1988]: the caudate (C), putamen (P), globus pallidus (G) and thalamus (T). To the right, deep gray matter internal nuclei as seen in a normal T1 weighted axial MR image with good contrast between WM, GM and CSF.

Registration to a digital atlas has become a common technique with the introduction of popular statistical algorithms for image processing, such as Statistical Parametric Mapping (SPM) [Ashburner and Friston 2000] or Expectation Maximization Segmentation (EMS) [Van Leemput et al. 2001]. A widely-used probabilistic atlas is the MNI Atlas from the Montreal Neurological Institute at McGill University [Collins et al. 1998]. It was built using over 300 MRI scans of healthy individuals to compute an average brain MR image, the MNI template, which is now the standard template of SPM and the International Consortium for Brain Mapping [Mazziotta et al. 2001]. However the averaging is performed on the entire brain and the three main tissue classes: GM, WM and CSF. More anatomical details can be found in manually segmented brain scans, and popular or new options are the Zubal Atlas from Yale University [Zubal et al. 1994], the SPL Atlas from Harvard Medical School [Kikinis et al. 1996], the basal ganglia atlas build from histological data from Pitié-Salpêtrière Hospital in Paris [Yelnik et al. 2007] and IBSR from Massachusetts General Hospital, Harvard Medical School, which is employed in this work.

1.4. Gray Nuclei Segmentation

The challenging nature of the problem of segmenting gray matter nuclei from MRI images stems from the lack of contrast, limitations of image resolution, and possible imaging artifacts. Few works have attempted to provide a fully automated algorithm for their identification and accurate delineation. [Dawant et al. 1999] propose a method for the

segmentation of internal brain structures based on similarity and free-form deformations to register one segmented image. No statistical atlas information is employed for spatial normalization. [Joshi et al. 2004] propose a method for unbiased diffeomorphic atlas construction, and they show results on the segmentation of the caudate nucleus within the context of a study on autism. [Pohl et al. 2006] propose a method for joint segmentation and registration based on the Expectation-Maximization (EM) algorithm, and apply their method to the segmentation of the thalamus.

We propose digital atlases that deform to fit the image data to be analyzed. Our fully automatic technique is based on a combination of rigid, affine and non-linear registration. A priori information on key anatomical landmarks is used to propagate the information from the atlas employing the computed deformation field. The technique offers the robust segmentation and quantification of difficultly identifiable brain structures in conjuncture with deformable atlases.

2. METHODS

2.1. Data

For the analysis of deep gray nuclei in this chapter, we used the Internet Brain Segmentation Repository[1] (IBSR) from the Center for Morphometric Analysis, Massachusetts General Hospital, Harvard Medical School. Boston, MA. The database consists of 18 high-resolution T1 MR scans of normal subjects. For each scan, 43 individual brain structures, including the deep gray nuclei, are manually segmented. The MR image data are T1-weighted 3D coronal acquisitions. The image resolution is between 0.93x0.93x1.5 mm^3 and 1x1x1.5 mm^3. There are 4 female and 14 male datasets with ages between juvenile and 71 years, covering a large variability of brain anatomies. A subject image from the IBSR database is shown in Figure 2. T1-weighted volumetric images from IBSR have been positionally normalized into the Talairach orientation (rotation only). This rigid transformation provides a first level of inter-subject alignment.

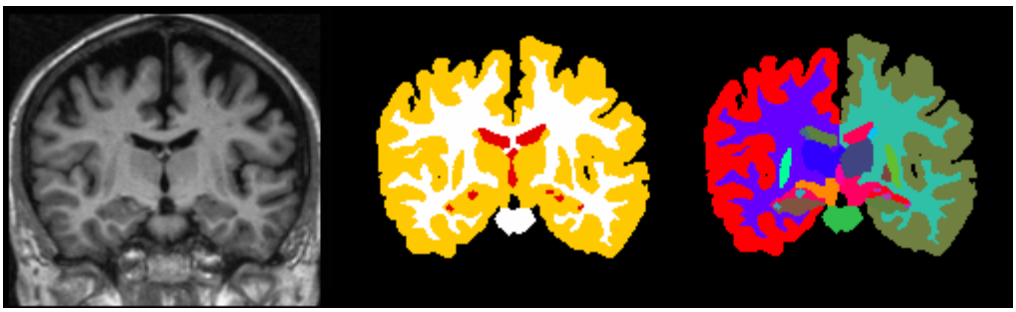

Figure 2. The IBSR database. We present a case from the ISBR database: from left to right, the coronal MR T1 scan; the segmentation of WM (white), GM (yellow) and CSF (red); the map of the manually segmented 43 brain structures.

[1] http://www.cma.mgh.harvard.edu/ibsr/

2.2. Spatial Normalization

The large variability inherent to human anatomy and the differences in patient positioning across scans leads us to consider further spatial normalization for the identification of deep gray nuclei. This will allow localizing the areas of interest with the help of an atlas of the brain. Furthermore, it will make automatic inter-patient comparisons possible.

For the construction of the statistical atlas, we chose using the data from IBSR, as it contains 18 manually segmented scans; they can provide the level of necessary information to guide the segmentation of brain structures, but also be used for the quantitative validation of the segmentation method. Given that the IBSR images are already aligned rigidly to the Talairach space, we perform a first refinement of the rigid registration using an affine transform. One random image from the database is selected as atlas. The atlas selection may introduce a bias, as the chosen atlas is not an average morphology and the segmentation does not account for intra-observer variability. The atlas T1-weigthed scan is registered to each of the other 17 T1 scans. We employ a robust block-matching algorithm to estimate the affine deformation between subjects' scans. [Ourselin 2000, Ourselin 2001].

The block matching strategy is a two-step iterative method. The standard assumption behind the algorithm is that there is a global intensity relationship between the template or reference image, *I,* and the one being registered to it or floating image, *J*. The result is reflected by the registered image $J' = J \circ T$, with T being the registration transformation.

In the first step, each block of I, B_I, is locally translated over J and a correlation coefficient CC is maximized to blocks of J, B_J. We use a correlation coefficient, as the registration is performed between monomodal T1-weighted MR images.

$$CC(B_I, B_J) = \frac{1}{N^2} \sum_{i,j} \left[\frac{(x_i - \mu_{B_I})(y_i - \mu_{B_J})}{\sigma_{B_I} \sigma_{B_J}} \right],$$

where x_i are elements of B_I, y_j are elements of B_J, and by μ and σ we denote the mean values and standard deviations.

Thus, the transformation between the two images is computed block by block and a displacement field is generated after removing outliers. In the second step, a parametric transformation, in this case affine, is estimated by regularizing the deformation field to explain most of the block correlations. A least trimmed squared regression approximates the affine transformation by minimizing the residual error

$$\min_T \sum_i \left\| r_{i:n} \right\|^2,$$

where $\left\| r_{i:n} \right\|^2$ are the squared ordered Euclidean residual norms $r_i = B_{I_i} - T(B_{J_i})$ and n is the number of displacement vectors.

To improve robustness, this procedure is repeated iteratively at multiple scales. Resulting registered data are interpolated using a linear function. More details can be found in [Ourselin

2001]. The alignment of the atlas to all individual scans allows a more robust inter-subject analysis and statistical algorithms can be applied.

2.3. Refined Segmentation

To be able to segment GM and WM in MRI data, a good contrast between these types of tissue in T1-weighted images is desired. Although image acquisition has radically improved over the last years, the variation in parameters and patient motion brings artifacts and variations in image appearance. Bias field inhomogeneities further contribute to the degradation of image quality. Hence, the segmentation of GM cannot be done reliably only from the patient images.

An affine transformation provides a better level of inter-subject GM alignment than a rigid transformation. However, to segment small GM sub-structures a more precise registration is necessary. For the examples in this chapter, we will focus on the basal ganglia. Hence, we create a mask with the caudate, globus pallidus, thalamus and putamen, which will be referred as internal nuclei for the rest of this paper, from the atlas (Figure 3). We aim to use this mask for the segmentation of internal nuclei in the other subject images.

Non-linear (free-form) registration is used to align the T1 scans of the affinely registered atlas and the corresponding T1 images of the 17 subjects. We employ a diffeomorphic non-linear registration algorithm based on Thirion's demons algorithm [Thirion 1998; Vercauteren et al. 2007a; Vercauteren et al. 2007b]. This algorithm has an open-source implementation [Vercauteren et al. 2007c] and is used in the free MedINRIA v 1.6.0 package[2] from the Asclepios Research Group, INRIA [Toussaint et al. 2007].

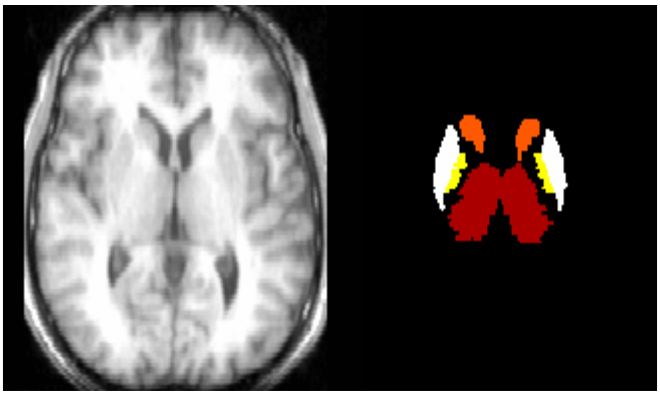

Figure 3. The mask of internal nuclei. We show an axial view of the T1 image chosen as atlas and the corresponding mask of manually segmented basal ganglia, including the caudate (orange), globus pallidus (yellow), putamen (white) and thalamus (red).

It has been shown in [Pennec et al. 99] that the demons algorithm could be seen as an optimization of a global energy. The main idea is to introduce a hidden variable in the registration process: correspondences. We then consider the regularization criterion as a prior on the smoothness of the transformation *T*. Instead of requiring that point correspondences

[2] http://www-sop.inria.fr/asclepios/software/MedINRIA/

between image pixels (a vector field C) be exact realizations of the transformation, one allows some error at each image point. Given the template image I and the floating image J, we end up with the global energy

$$E(C,T) = \sigma_i^{-2}\,\mathrm{Sim}(I, J\circ C) + \sigma_x^{-2}\,\mathrm{dist}(T,C)^2 + \sigma_T^{-2}\,\mathrm{Reg}(T)\,,$$

$$\mathrm{Sim}(I, J\circ C) = \frac{1}{2}\left\|I - J\circ C\right\|^2\,,$$

where σ_i accounts for the noise on the image intensity, σ_x for a spatial uncertainty on the correspondences, and σ_T controls the amount of regularization we need. We classically have $\mathrm{dist}(T,C) = \|C\text{-}T\|$ and $\mathrm{Reg}(T) = \|\nabla T\|^2$, but the regularization can also be modified to handle fluid-like constraints [Cachier et al. 2003].

Within this framework, the demons registration can be explained as an alternate optimization over T and C. The optimization is performed within the complete space of dense non-linear transformations by taking a series of additive steps, $T \leftarrow T+\boldsymbol{u}$. The most straightforward way to adapt the demons algorithm to make it diffeomorphic is to optimize $E(C,T)$ over a space of diffeomorphisms. This can be done as in [Malis 2004; Mahony et al. 2002] by using an intrinsic update step

$$T \leftarrow T \circ \exp(\boldsymbol{u})\,,$$

on the Lie group of diffeomorphisms. This approach requires an algorithm to compute the exponential for the Lie group of interest. Thanks to the scaling and squaring approach in [Arsigny et al. 2006], this exponential can efficiently be computed for diffeomorphisms with just a few compositions:

Algorithm (Fast Computation of Vector Field Exponentials).

- Choose N such that $2^{-N}\boldsymbol{u}$ is close enough to 0, e.g. $\max_p \|2^{-N}\boldsymbol{u}(p)\| \leq 0.5$;
- Perform an explicit first order integration: $v(p) \leftarrow 2^{-N}\boldsymbol{u}(p)$ for all pixels;
- Do N (not $2N$!) recursive squarings of v: $v \leftarrow v \circ v$.

By plugging the Newton method tools for Lie groups within the alternate optimization framework of the demons, we proposed in [Vercauteren et al. 2007a] the following non-parametric diffeomorphic image registration algorithm:

Algorithm (Diffeomorphic Demons Iteration).

- Compute the correspondence update field $\boldsymbol{u}$ using a regular demons step;
- If a fluid-like regularization is used, let $\boldsymbol{u} \leftarrow K_{\mathrm{fluid}} * \boldsymbol{u}$;
- Let $C \leftarrow T\circ\exp(\boldsymbol{u})$, where $\exp(\boldsymbol{u})$ is computed using the above fast algorithm;
- If a diffusion-like regularization is used, let $T \leftarrow Id + K_{\mathrm{diff}} * (C\text{-}Id)$ (else let $T \leftarrow C$).

Having the deformation fields computed, we apply them to the mask of internal nuclei of the atlas, deforming the mask according to the position and size of the internal nuclei in each subject image. A diagram of the algorithm is shown in Figure 4. The deformed mask is used to segment the internal nuclei of the patient, namely the caudate, globus pallidus putamen, putamen and thalamus.

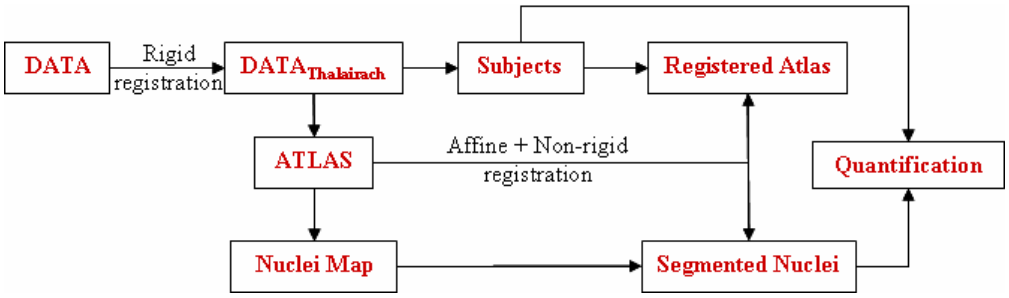

Figure 4. Diagram of the algorithm for segmentation and quantification of the brain deep gray matter nuclei.

In order to preserve the correct values of the segmentation labels posterior to the application of the transformation, nearest-neighbor interpolation is performed, as opposed to the case of patient image registration, which employed linear interpolation.

2.4. Quantification

For each internal nucleus, we compute a segmentation overlap between the automatic and the manual segmentations as a quantifiable measure of the success of the algorithm. The metric for validation is based on the Dice Coefficient (DC)

$$DC = \frac{2|S_A \cap S_M|}{|S_A| + |S_M|},$$

where S_A is the segmented region of the automatic method, and S_M is the manually segmented region by an expert.

The volume estimation between manual and automatic volume measurement is computed for each type of internal nucleus. To correlate the manual and automatic estimates, we use the R-squared (R^2) value of the best linear fit of data correlation

$$R^2(V_A, V_M) = \frac{\mathrm{cov}(V_A, V_M)}{\sigma_{V_A}\sigma_{V_B}},$$

where cov represents the covariance between the manual (V_M) and automatic (V_A) estimates of nucleus volume and σ the standard deviation.

3. RESULTS

You will note that we present our results alternating between coronal and axial views. Images in the IBSR database are acquired in a coronal view, but for visualization we show them in radiological convention view as well.

We compared registration results at three levels of deformation: rigid, affine and non-linear. Figure 5 presents one subject scan and the atlas being deformed to best match the subject. The rigid registration on the Thalairach space provides a good alignment, but does not handle any anatomical differences. The affine transformation is better suited for the registration, but still insufficient to align small structures, such as the internal nuclei. Finally, the non-linear refinement provides the best fit between the two 3D images. Note the adaptation of size and shape of the ventricles and thalamus.

Checkerboard comparative images for the three levels of registration are presented in Figure 6 for a better visual assessment. Note the better correspondence between brain structures after non-linear registration. Hence, we save the non-linear transformation field presented in Figure 7 and apply it to the mask of internal nuclei (Figure 3).

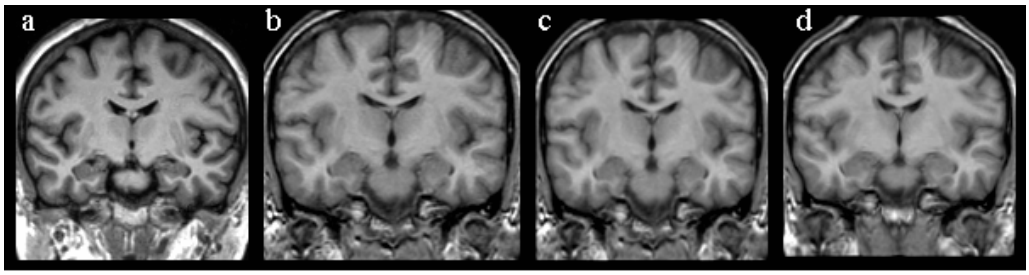

Figure 5. Inter-patient registration: (a) the target image; (b) the source image after rigid registration; (c) the source image after affine registration; (d) the deformed source using non-linear registration.

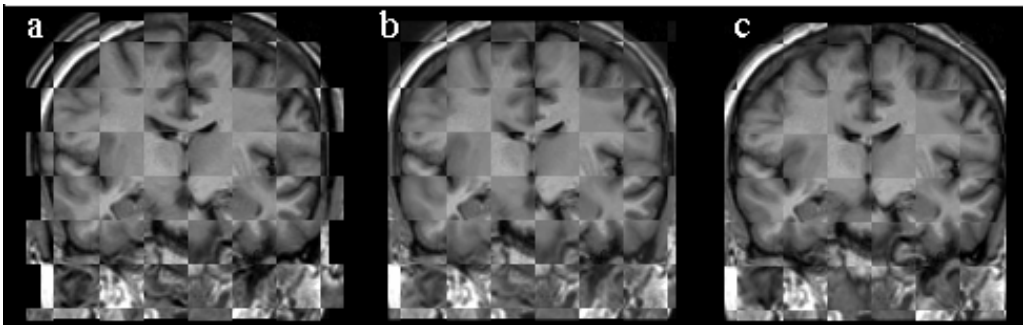

Figure 6. Comparative registration results using checkerboards: (a) after rigid registration (b) after affine registration; and (c) using non-linear transformations;

Segmentation results for the group of deep gray matte nuclei (caudate, globus pallidus, putamen and thalamus) are illustrated in Figure 8. For visual assessment of the impact of the registration on segmentation, the results are shown after rigid, affine and non-linear registration and compared to the manual segmentation of nuclei. Segmented nuclei mask are overlaid on the T1 scans of the subject. Once more, we observe the superior segmentation

provided after non-linear registration. In Figure 9 we present difference images between nuclei mask using automatic and manual segmentations. The error in volume estimation using non-linear registration is significantly smaller than using transformations with fewer degrees of freedom.

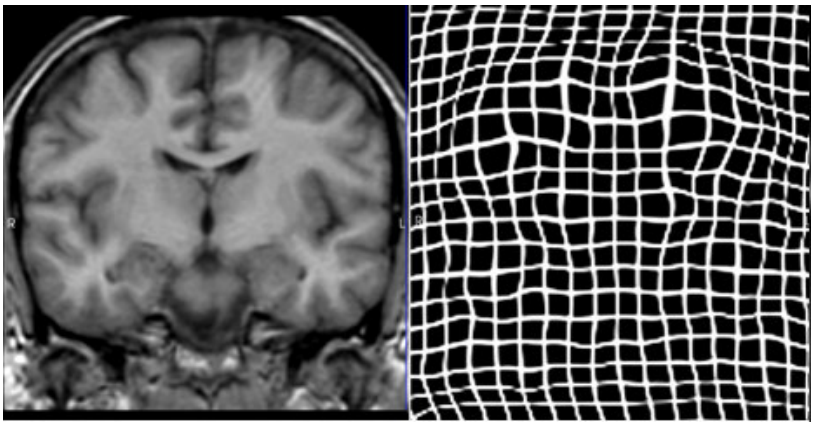

Figure 7. Deformation fields. We present the source image (atlas) used in the registration and the deformation filed resulting from the non-linear registration to the target image.

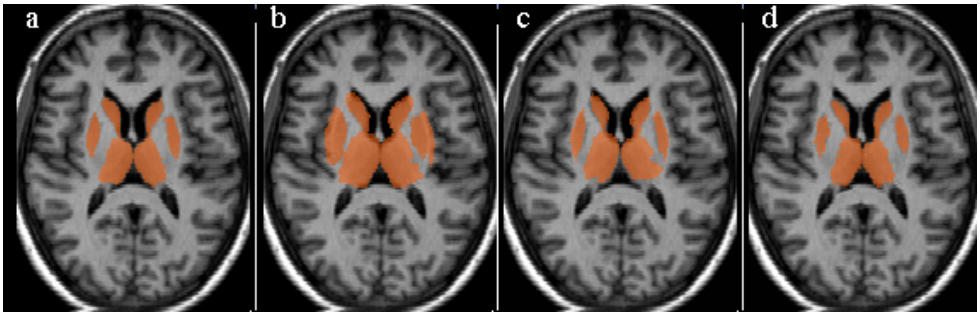

Figure 8. Segmentation of gray nuclei: (a) the manual segmentation; (b) after rigid registration; (c) using affine registration; and (d) using the non-linear transformation fields.

Figure 9. Segmentation overlap with the manual segmentation: (a) the difference image after rigid registration; (b) after affine registration; and (c) using non-linear registration.

More segmentation results using non-linear registration are shown in Figure 10 and 11.

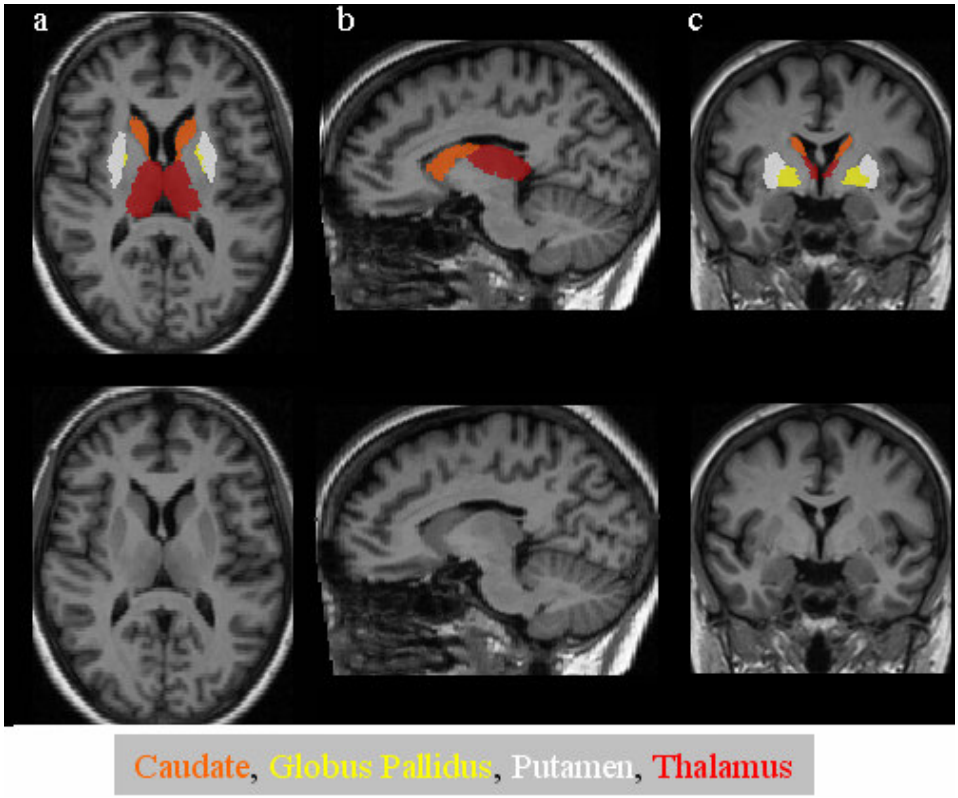

Figure 10. Segmentation of gray nuclei in radiological convention. We present segmentation results in axial (a), sagittal (b) and coronal (c) views. The bottom row shows the MR image for the visual evaluation of the automatic segmentation results.

Figure 10 shows typical segmentation results in a subject scan. We separate the nuclei using a color code: orange for caudate, yellow for globus pallidus, white for putamen and red for thalamus. Axial, sagittal and coronal views are presented for 3D assessment. In Figure 11 we browse through the 3D coronal space of the subject and compare the manual and automatic segmentation of the four internal nuclei. Finally, a 3D map of the segmented nuclei is illustrated in Figure 12 using 3D rendering.

To quantify the quality of the segmentation for the 17 subject data, the overlap ratios and errors in volume estimation between the manual and automatic segmentations were computed. Values were calculated for each type of nuclei (caudate, globus pallidus, putamen and thalamus) and for all nuclei together, as denominated by gray nuclei. Numerical figures are presented in Table 1. As expected, numbers look better for the larger nuclei, as they are correlated with the structure size. The charts of the overlap ratio and error of volume estimation are seen in Figure 13 and Figure 14 respectively.

The correlations between manual and automatic segmentation is presented in Figures 15 and 16. Figure 15 shows the best linear fit of the correlated data and the R-squared (R^2) value for each category of nuclei (caudate, globus pallidus, putamen and thalamus). In Figure 16 we present the correlation for all internal nuclei together.

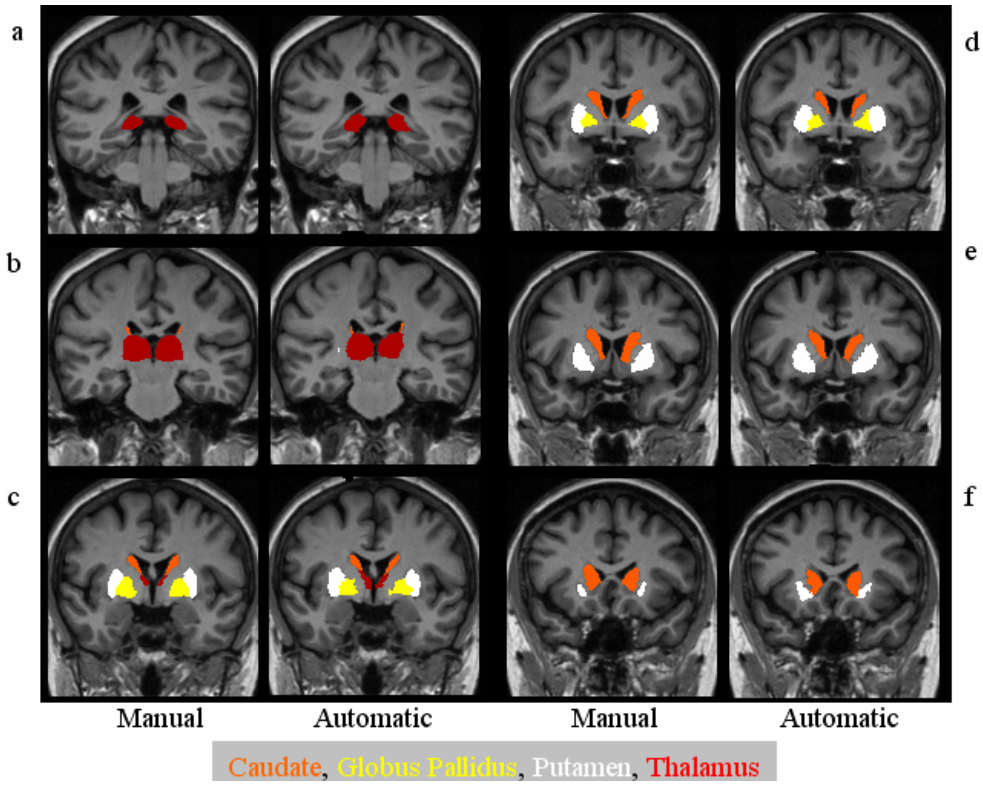

Figure 11. 3D segmentation of nuclei. We present comparative results between the manual and automatic segmentations of deep gray nuclei at six coronal locations along the 3D volume of the brain.

Figure 12. A 3D map of the segmented gray nuclei.

Table 1. Segmentation error. The rows present the overlap ratio and volume estimation error for four categories of gray nuclei (caudate, globus pallidus, putamen and thalamus) and the total volume of the nuclei (gray nuclei)

	Caudate	Globus Pallidus	Putamen	Thalamus	Gray Nuclei
Overlap ratio	0.824±0.038	0.788±0.045	0.855±0.023	0.883±0.033	0.855±0.018
Volume error (%)	9.59±4.268	11.112±7.02	4.387±2.348	3.299±2.078	2.613±2.058

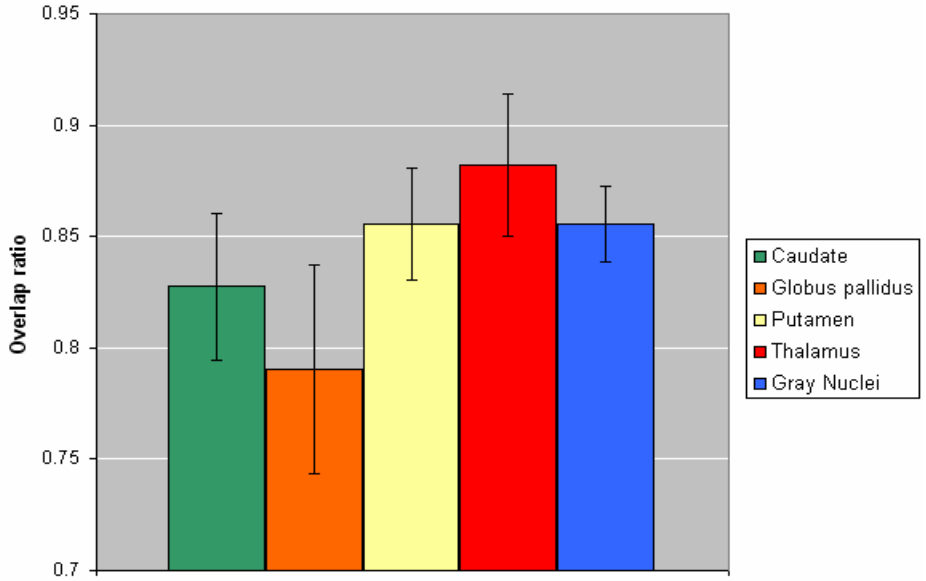

Figure 13. The computed overlap between manual and automatic segmentation of deep nuclei of the brain. The bar corresponding to "gray nuclei" refers to the combined volume of caudate, globus pallidus, putamen and thalamus.

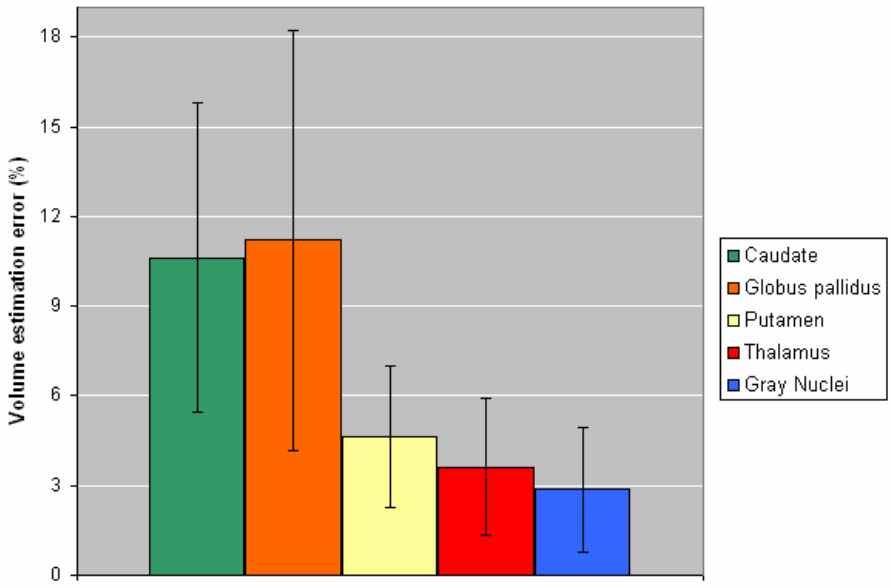

Figure 14. The computed error in volume estimation between manual and automatic segmentation of deep nuclei of the brain.

It has been shown that the error induced by MRI partial volume effects in small structures can be in the range 20-60 % of the volume [González Ballester et al. 2000]. Taking into account the size of grey matter nuclei and the good correlation with manual segmentations, our results show the suitability of our approach for neuroanatomical studies.

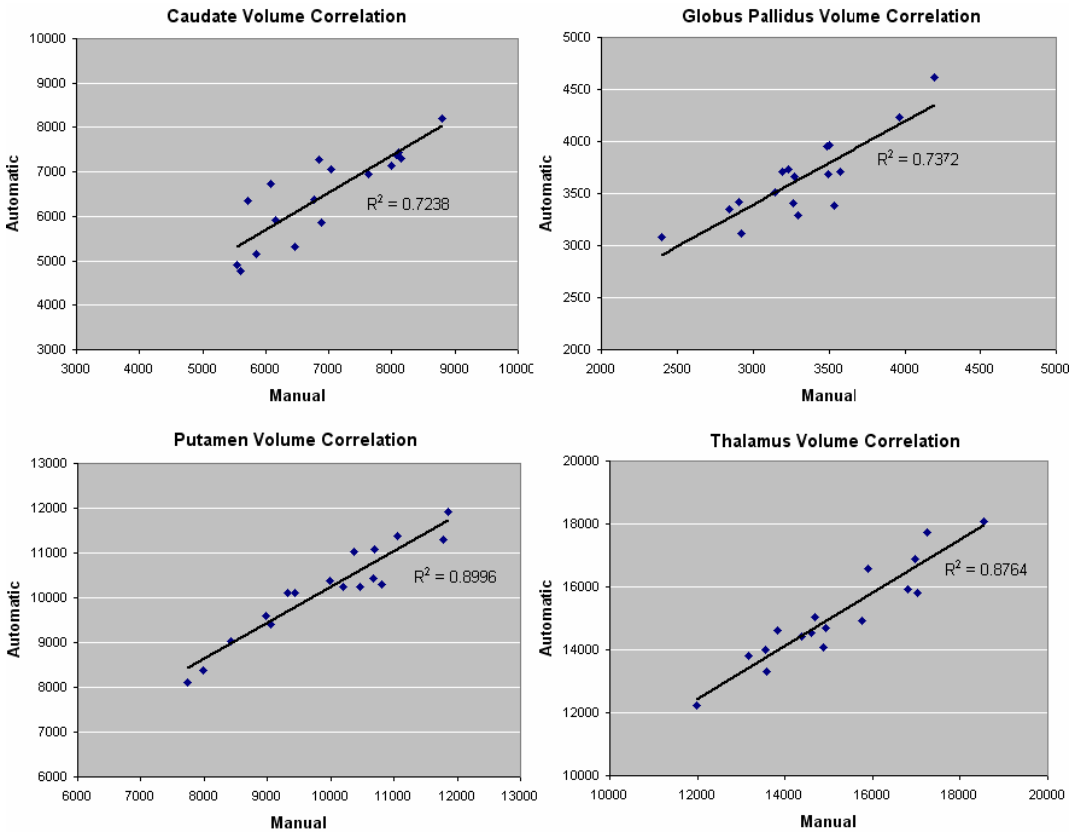

Figure 15. The best linear fits and R-squared values for correlated volume estimations of the four categories of gray nuclei. The horizontal axes correspond to the manual segmentation, and the automatic segmentation estimates are shown on the vertical axes.

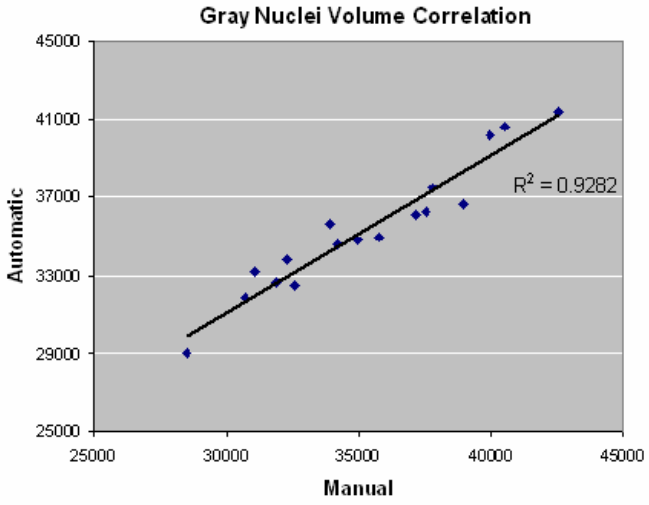

Figure 16. The best linear fit and R-squared value for correlated volume estimations of the total volume of the segmented gray nuclei: caudate, globus pallidus, putamen and thalamus.

Given the high resolution and good contrast in the IBSR images, the inter-subject registration of T1-weighted MR images is sufficiently robust to govern the segmentation of small internal nuclei. However, in clinical practice data quality is variable and the intensity information from MRI may be inadequate to find an accurate alignment between scans. In these situations, it is desirable to use anatomical landmarks for the definition of more precise transformations. We proposed to employ easily identifiable anatomical structures in the brain, such as the lateral ventricles and cortex boundary. For more detail please refer to [Linguraru et al. 2006; Linguraru et al. 2007].

CONCLUSION

We proposed digital atlases that deform to fit the image data to be analyzed. Our fully automatic technique is based on a combination of rigid, affine and non-linear registration. A priori information on anatomical landmarks was used to propagate the information from the atlas employing the computed deformation field. The technique offers the robust segmentation and quantification of difficultly identifiable brain structures in conjuncture with deformable atlases.

In this chapter, we focused on the segmentation of the basal ganglia to present our algorithm for the segmentation of deep gray matter nuclei. An identical approach can be used for other inner brain structures to accurately segment them in patient images.

REFERENCES

Ashburner J, Friston KJ. Voxel-based morphometry--the methods. *Neuroimage*. 2000 Jun;11(6 Pt 1):805-21.

Brown MA, Semelka RC. MR imaging abbreviations, definitions, and descriptions: a review. *Radiology*. 1999 Dec;213(3):647-62.

Cachier P, Bardinet E, Dormont D, Pennec P, Ayache N. Iconic feature based nonrigid registration: The PASHA algorithm. *Computer vision and image understanding*. 2003 Feb; 89(2-3):272-298.

Collins DL, Zijdenbos AP, Kollokian V, Sled JG, Kabani NJ, Holmes CJ, Evans AC. Design and construction of a realistic digital brain phantom. *IEEE Trans Med Imaging*. 1998 Jun;17(3):463-8.

Dawant BM, Hartmann SL, Thirion JP, Maes F, Vandermeulen D, Demaerel P. Automatic 3-D segmentation of internal structures of the head in MR images using a combination of similarity and free-form transformations: Part I, Methodology and validation on normal subjects. *IEEE Trans Med Imaging*. 1999 Oct;18(10):909-16.

Duncan J, Ayache N. Medical Image Analysis: Progress over Two Decades and the Challenges Ahead. *IEEE Transactions on Pattern Analysis and Machine Intelligence* 2000; 22(1):85-106.

Fennema-Notestine C, Ozyurt IB, Clark CP, Morris S, Bischoff-Grethe A, Bondi MW, Jernigan TL, Fischl B, Segonne F, Shattuck DW, Leahy RM, Rex DE, Toga AW, Zou KH, Brown GG. Quantitative evaluation of automated skull-stripping methods applied to contemporary and legacy images: effects of diagnosis, bias correction, and slice location. *Hum Brain Mapp.* 2006 Feb; 27(2):99-113.

González Ballester MA, Zisserman AP, Brady M. Segmentation and measurement of brain structures in MRI including confidence bounds. *Med. Image Anal*. 2000; 4(3):189-200.

González Ballester MA, Zisserman AP, Brady M. Estimation of the partial volume effect in MRI. *Med. Image Anal*. 2002 Dec;6(4):389-405.

Guillemaud R, Brady M. Estimating the bias field of MR images. *IEEE Trans Med. Imaging*. 1997 Jun;16(3):238-51.

Han X, Jovicich J, Salat D, van der Kouwe A, Quinn B, Czanner S, Busa E, Pacheco J, Albert M, Killiany R, Maguire P, Rosas D, Makris N, Dale A, Dickerson B, Fischl B. Reliability of MRI-derived measurements of human cerebral cortical thickness: the effects of field strength, scanner upgrade and manufacturer. *Neuroimage.* 2006 Aug 1;32(1):180-94.

Hornak JP. The Basics of MRI, http://www.cis.rit.edu/htbooks/mri/

Joshi S, Davis B, Jomier M, Gerig G. Unbiased diffeomorphic atlas construction for computational anatomy. *Neuroimage*. 2004;23 Suppl 1:S151-60.

Kikinis R, Shenton ME, Iosifescu DV, McCarley RW, Saiviroonporn P, Hokama HH, Robatino A, Metcalf D, Wible CG, Portas CM, Donnino RM, Jolesz FA. A digital brain atlas for surgical planning, model-drivensegmentation, and teaching. *IEEE Transactions on Visualization and Computer Graphics* 1996; 2(3):232-41.

Linguraru MG, Ayache N, Bardinet E, Ballester MA, Galanaud D, Haïk S, Faucheux B, Hauw JJ, Cozzone P, Dormont D, Brandel JP. Differentiation of sCJD and vCJD forms by automated analysis of basal ganglia intensity distribution in multisequence MRI of the brain--definition and evaluation of new MRI-based ratios. *IEEE Trans Med Imaging.* 2006 Aug;25(8):1052-67.

Linguraru MG, Gonzalez Ballester MA, Ayache N. Deformable Atlases for the Segmentation of Internal Brain Nuclei in Magnetic Resonance Imaging. *International Journal of Computers, Communication and Control* 2007;2(1):26-36.

Mahony R, Manton J.H.. The geometry of the Newton method on non-compact Lie-groups. *Journal of Global Optimization*. 2002 Aug; 23(3):309-27.

Malis E. Improving vision-based control using efficient second-order minimization techniques. *IEEE Int. Conf. Robot Automat*. 2004.

Mazziotta J, Toga A, Evans A, Fox P, Lancaster J, Zilles K, Woods R, Paus T, Simpson G, Pike B, Holmes C, Collins L, Thompson P, MacDonald D, Iacoboni M, Schormann T, Amunts K, Palomero-Gallagher N, Geyer S, Parsons L, Narr K, Kabani N, Le Goualher G, Boomsma D, Cannon T, Kawashima R, Mazoyer B. A probabilistic atlas and reference system for the human brain: International Consortium for Brain Mapping (ICBM). *Philos. Trans R Soc. Lond B Biol. Sci.* 2001 Aug 29;356(1412):1293-322.

Ourselin S, Roche A, Prima S, Ayache N. Block matching: a general framework to improve robustness of rigid registration of medical images. In: DiGioia AM, Delp S editors. *Medical Robotics, Imaging and Computer Assisted Surgery (MICCAI 2000).* Lectures Notes in Computer Science 1935, Berlin Heidelberg: Springer 2000; 557-566.

Ourselin S, Roche A, Subsol G, Pennec X, Ayache N. Reconstructing a 3D structure from serial histological sections. *Image and Vision Computing* 2001;19(1-2):25-31.

Pennec X, Cachier P, Ayache N. Understanding the demon's algorithm: 3D non-rigid registration by gradient descent. . *Med Image Comput Comput Assist Interv Int Conf Med Image Comput Comput Assist Interv*. 1999; 597-605.

Pohl KM, Fisher J, Grimson WE, Kikinis R, Wells WM. A Bayesian model for joint segmentation and registration. *Neuroimage*. 2006 May 15;31(1):228-39.

Sled JG, Zijdenbos AP, Evans AC. A nonparametric method for automatic correction of intensity nonuniformity in MRI data. *IEEE Trans Med Imaging*. 1998 Feb;17(1):87-97.

Summerfield C, Junqué C, Tolosa E, Salgado-Pineda P, Gómez-Ansón B, Martí MJ, Pastor P, Ramírez-Ruíz B, Mercader J. Structural brain changes in Parkinson disease with dementia: a voxel-based morphometry study. *Arch. Neurol*. 2005 Feb;62(2):281-5.

Stark DD, Bradley WG, Bradley JR. WG. Magnetic Resonance Imaging. St Louis, Mosby 1999.

Talairach J, Tournoux P. Co-Planar Stereotaxic Atlas of the Human Brain. New York, Thieme Medical Publishers 1988.

Thirion JP. Image matching as a diffusion process: an analogy with Maxwell's demons. *Med Image Ana*l. 1998 Sep;2(3):243-60.

Toussaint N, Souplet J-C, Fillard P. MedINRIA : Medical image navigation and research tool by INRIA. *MICCAI'07 Workshop on Interaction in Medical Image Analysis and Visualization.* 2007.

Van Leemput K, Maes F, Vandermeulen D, Colchester A, Suetens P. Automated segmentation of multiple sclerosis lesions by model outlier detection. *IEEE Trans Med. Imaging*. 2001 Aug;20(8):677-88.

Van Leemput K, Maes F, Vandermeulen D, Suetens P. Automated model-based bias field correction of MR images of the brain. *IEEE Trans Med Imaging.* 1999 Oct;18(10):885-96.

Vercauteren T, Pennec X, Malis E, Perchant A, Ayache N. Insight into efficient image registration techniques and the demons algorithm. *Inf. Process Med. Imaging.* 2007a;20:495-506.

Vercauteren T, Pennec X, Perchant A, Ayache N. Non-parametric diffeomorphic image registration with the demons algorithm. *Med. Image Comput Comput Assist Interv Int. Conf Med. Image Comput. Comput Assist Interv.* 2007b;10(Pt 2):319-26

Vercauteren T, Pennec X, Perchant A, Ayache N. Diffeomorphic Demons Using ITK's Finite Difference Solver Hierarchy. *Insight Journal*, ISC/NA-MIC Workshop on Open Science at MICCAI 2007. 2007c.

Yelnik J, Bardinet E, Dormont D, Malandain G, Ourselin S, Tandé D, Karachi C, Ayache N, Cornu P, Agid Y. A three-dimensional, histological and deformable atlas of the human basal ganglia. I. Atlas construction based on immunohistochemical and MRI data. *Neuroimage*. 2007 Jan 15;34(2):618-38.

Zubal IG, Harrell CR, Smith EO, Rattner Z, Gindi G, Hoffer PB. Computerized three-dimensional segmented human anatomy. *Med. Phys.* 1994 Feb;21(2):299-302.